Simulation of dendritic grain structures with Cellular Automaton–Parabolic Thick Needle model

Y. Wu, O. Senninger, Ch.-A. Gandin

Simulation of dendritic grain structures with Cellular Automaton - Parabolic Thick Needle model

Y. Wu [(1)], O. Senninger [(1)*], Ch.-A. Gandin[(1)]

(1) Mines Paris, PSL University, Center for material forming (CEMEF), UMR CNRS, 06904 Sophia Antipolis, France

Abstract

This article presents advances and computing optimizations on the CAPTN model which couples the Cellular Automaton (CA) and the Parabolic Thick Needle (PTN) methods. This optimized CAPTN model, which is developed in 2D for now, is evaluated on its ability to reproduce two physical quantities developed during directional growth in a constant temperature gradient G with isotherm velocity v_L: the interdendritic primary spacing and the grain boundary orientation angle between two grains of different orientations. It is shown that the CAPTN model can reproduce selection between primary branches and creation of new branches from tertiary branches as long as cell size is sufficiently small to model solute interactions between branches. In these conditions, simulations converge toward a distribution of primary branches which depends on the history of the branching events, as has been observed in ~~in agreement with~~ experimental ~~results~~ studies. Average primary spacing obtained tend to decrease with G and v_L, in agreement with ~~and~~ the theoretical $G^{-b}v_L^{-c}$ power law. Contrary to the classical CA model, the grain boundary orientation angle obtained in CAPTN simulations is stable with cell size and in good agreement with previous phase field studies for various gradients. Moreover, the grain boundary orientation angle is found to follow an exponential law with the ratio G/v_L.

Keywords: dendritic growth; modeling; CAPTN model; primary dendrite arm spacing; grain boundary orientation

*Corresponding author

Email address: oriane.senninger@minesparis.psl.eu (O. Senninger [(1)])

Graphical abstract

Solidification front at t=300 s for a bi-crystal CAPTN simulation of succinonitrile – 1.3wt% acetone alloy with G=0.475 K.mm^{-1}, v_L=0.086 mm.s^{-1} andl l_{CA}=0.2 mm

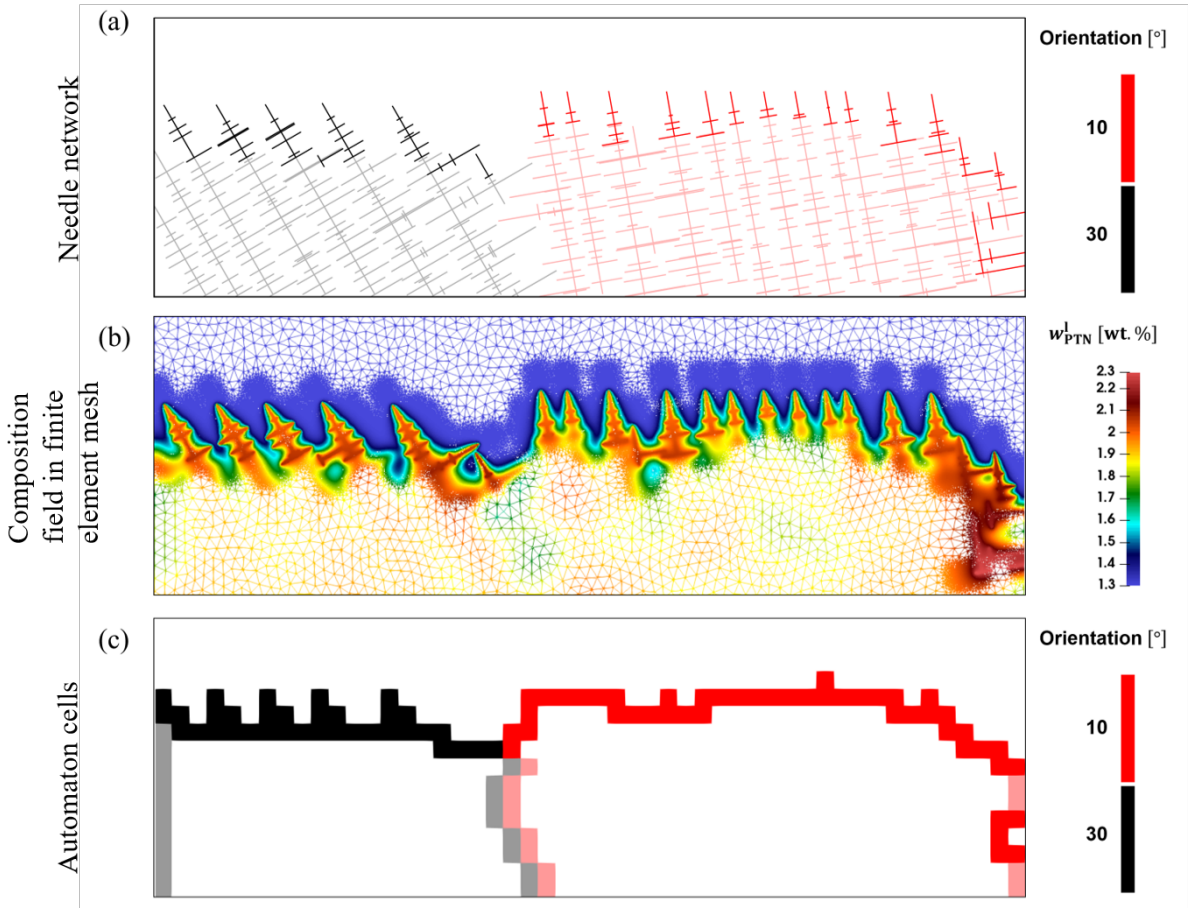

1. Introduction

The prediction of dendritic microstructures formed during metal solidification processes is of major scientific and industrial interest [1]. Intragranular quantities such as the primary dendrite arm spacing and intergranular quantities such as the grain size and the direction of grain boundaries have consequences on the thermo-mechanical properties of manufactured parts. Modeling the formation of dendritic structures makes it possible to understand and predict how the solidification conditions influence these characteristic scales. However, the physical phenomena governing these characteristic scales extend over large spatial scales, requiring choices in the approximations and dimensions of the numerical models chosen.

Phase field (PF) models are currently the models with the finest resolution of dendritic structures [2, 3, 4]. However, these models are very expensive numerically and are limited to ~~small~~ simulation domains of the order of 0.1 mm^3. Moreover, PF simulations can usually not achieve quantitative predictions of non-dilute alloys due to the large separation of scale between tip radius and diffusion length [5].

The Dendritic Needle Network (DNN) and the Parabolic Thick Needle (PTN) methods aim to overtake these numerical limits by approximating dendritic branches to ~~parabolas~~ paraboloids truncated by cylinders [6, 7, 8]. In this model, originally developed for solidification conditions such that a scale separation is feasible between tip radius and diffusion length (so at small Péclet number), solute diffusion and convection are solved in the liquid phase and dendrite tip growth velocities are computed from the integration of the solute composition gradient in the vicinity of dendrite tips. With the original methodologies, the DNN method is implemented on Graphics Processing Units (GPUs) using the finite difference method. Simulation domains can reach up to 100 mm^3 [9]. However, the solid fraction generated during grain growth was not modeled with this method and so the coupling of the microstructure evolution with thermal resolution was not achieved.

The so-called Cellular Automaton (CA) methods model the growth of dendritic grains on a grid of cells whose state evolves during the simulation from "liquid" to "growing" and then to "solid" state according to the local conditions of temperature, composition and the state of surrounding cells. In these approaches, we distinguish for this article the μCA models for which an intragranular resolution of the dendrites is performed and the CA models, which only model the growth of the grain envelope. For μCA models, the diffusion and solutal conservation equations are solved by finite difference at the scale of the cell grid. These models have shown their relevance for modeling the growth of columnar

grains by comparison with the LGK analytical model [10] and have been validated by comparison with theoretical and experimental studies on their modeling of secondary dendrite arm spacing [11]. However, like the PF method, these models require a fine spatial resolution which limits the dimensions of the simulated domains to domains of the order of 10^{-2} mm^3. CA models aim at predicting alloys grain structures by modeling the nucleation and growth of grain envelopes. Intragranular properties are thus not accessible with this approach. The grain envelopes develop on the CA grid. Within each CA cell, the dendritic microstructure is simplified by an orthodiagonal polygon (polyhedron in 3D), with half diagonals representing the length of the dendrite arms. For cubic crystal structures, these ~~Their~~ lengths are aligned with the $< 1\ 0 >$ (resp. $< 1\ 0\ 0 >$) in 2D (resp. 3D) directions [12]. Simulation domains can be as high as a few liters. The coupling between the grain structure developed during solidification and the thermal evolution of the simulated part can be modeled by coupling CA models with a finite element mesh in the CA-FE method [13]. However, at the cell scale, the growth kinetics of grain envelopes are approximated by analytical laws corresponding to stationary kinetics. These growth laws therefore do not take into account the solutal interactions between neighboring grains, which limits some quantitative agreement with experiments such as columnar/equiaxed transition [14].

The complementary advantages of the CA and PTN methods have motivated their coupling in the so called CAPTN model [15]. The PTN method is used to compute the dendrite tip velocity at the apices of the polygons (polyhedrons in 3D) of each CA cell. A first coupling has been performed in 2D with a FE implementation of the PTN model using adaptive mesh. It has been shown that this CAPTN method gives a description of equiaxed grain growth with a higher precision than the classical CAFE model. However, the strategy developed for the PTN implementation requires much heavier computational resources.

CA and PF models have been compared on their ability to predict the grain boundary orientation angle between two tilted grains in a temperature gradient moving at constant velocity in a two-dimensional domain [16]. It has been shown that the orientation angle of the grain boundary determined by the CA method depends on the CA cell size and is in agreement with the PF result if the mesh size corresponds to a quantity called "secondary dendrite arm spacing preceding tertiary branching".

In this article, the CAPTN method is evaluated on its ability to model two characteristic quantities resulting from the growth of dendritic grains placed in a constant tem-

perature gradient moving at constant speed: the primary dendrite arm spacing and the orientation angle of grain boundary between two grains of different orientations. Section 2 recalls the methodology of the CAPTN method and presents optimizations to drastically reduce the computational time of the method. A parametric study is performed in Section 3.1 to analyze the convergence of the model toward the theoretical kinetics in stationary state for an isolated dendrite tip. Sections 3.2 and 3.3 present the evaluation on the primary dendrite arm spacing and grain boundary orientation angle. Results are compared with CA and PF results. Finally, an exponential law on the evolution of the grain boundary orientation angle is proposed.

2. Model description

The CAPTN model uses a FE implementation of the PTN method for computing dendrite tip radius and velocity from liquid composition gradients in the vicinity of tips according to the method recalled in Section 2.1.1. Therefore, a fine mesh is required in the vicinity of each dendrite tip to compute its growth velocity with a good precision but a fine mesh cannot be applied on the whole domain without numerical cost. A first strategy of adaptive meshing has been proposed in Ref [15], with the application of a fine mesh at solid/liquid interfaces and with a mesh size following concentration gradients in the liquid phase. However, this meshing strategy requires to rebuild the mesh very frequently to keep track of the growing parabolic dendrite tips, which is numerically time consuming. In this paper, a new adaptive meshing strategy is proposed and described in Section 2.1.2. In Section 2.2 the methodology of coupling between the CA and PTN methods and improvements compared to the previous implementation are presented.

2.1. PTN finite element implementation

2.1.1. PTN theory and implementation

The PTN method [6, 7] is based on the approximation of dendrite branches as ~~parabolas~~ paraboloids of curvature radius ρ_{tip} truncated by cylinders of radius r_{cyl} (represented in light green in Fig 1 . In 2D, the truncation is caused by a rectangle, but to be consistent with 3D notations, the term "cylinder" is retained, and r_{cyl} is the half thickness of the rectangle). To compute the growth velocity of tips, v_{tip}, solute diffusion is solved in the liquid around tips to obtain the liquid composition field, w^l_{PTN}. For this, the composition at the nodes of the solid/liquid interfaces and inside paraboloids is imposed by a Dirichlet condition to the ~~liquid~~ liquidus composition w^{ls} corresponding to the temperature of the

tip, T_{tip}, i.e., $w^{ls} = (T_{tip} - T_M)/m$, where T_M is the melting temperature for the solvent, and m is the liquidus slope. As for the DNN model [7], the curvature undercooling is therefore negelected in the PTN model.

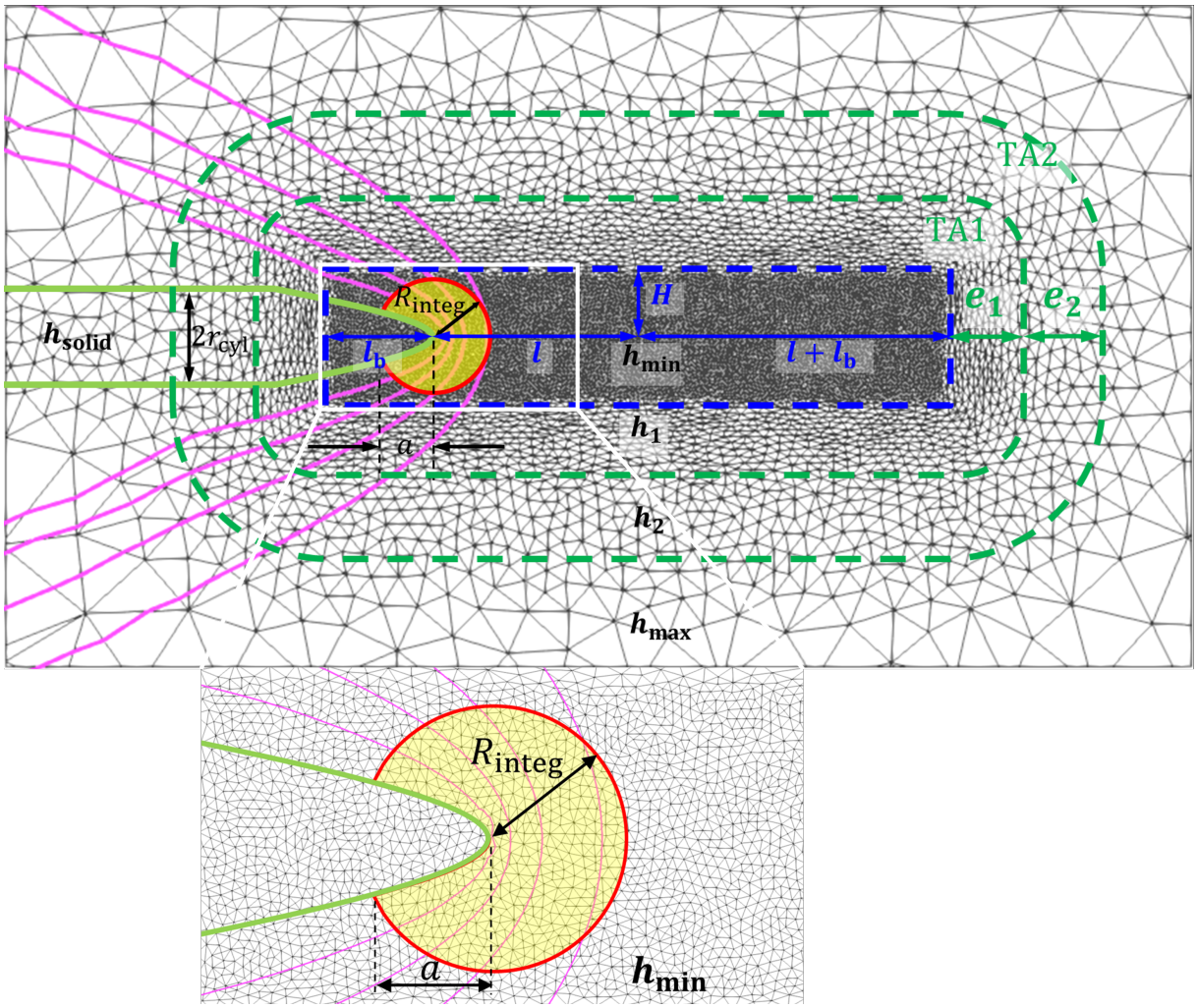

Figure 1: Sketch of the FE implementation of the PTN method. The truncated parabola (light green) moves in a liquid with solute isocomposition lines in pink. The integration area (surface Σ in yellow with its contour Γ in red) is a truncated disk of radius R_{integ} defined by the a parameter. The adaptive mesh generated for this branch is presented as a gray wireframe. The minimum mesh area with its dimensional parameters (l_b, l, and H) is delimited by the blue dashed box. The edges of the two transitional areas TA1 and TA2 of parameters e_1 and e_2 are marked with green dashed lines. The mesh size parameters h_{min}, h_{solid}, h_1, h_2, and h_{max} in each zone are written in black. A zoom of the area in the white box is shown at the bottom of the figure. Parameters a and h_{min} are discussed in Section 3.1.

Equations (1a) and (1b) give the relations between ρ_{tip} and v_{tip} in two dimensions:

$$\rho_{tip}^2 v_{tip} = \frac{D^l d_0}{\sigma} \tag{1a}$$

$$\rho_{tip} v_{tip}^2 = \frac{2\ D^{l2}\mathcal{F}^2}{d_0} \tag{1b}$$

where D^l is the interdiffusion coefficient in the liquid, $d_0 = -\Gamma^{ls}/m(1-k)w^{ls}$ is the solute capillary length, Γ^{ls} is the Gibbs-Thomson coefficient of the interface, and k is the segregation coefficient. The constant σ is the dendrite tip selection parameter. The quantity $\mathcal{F}$ in Eq. (1b) is called Flux Intensity Factor (FIF). To compute this quantity, an integration area of surface Σ (in yellow in Fig 1) and contour Γ (in red in Fig 1) ~~, parameterized with parameter a, which is the distance along the axis of the branch between the dendrite tip and the intersection of the contour Γ with the parabola,~~ is defined in front of the tip. This integration area is a disk of radius R_{integ} centered on the dendrite tip and truncated by the parabola. This disk is parameterized by parameter a, which is the distance along the axis of the branch between the dendrite tip and the intersection of the contour Γ with the parabola (see Fig 1). The scaling of this numerical parameter will be discussed in section 3.1. ~~with its tip located at the center of the disk.~~ The radius R_{integ} is therefore related to a by $R_{integ} = \sqrt{a^2 + 2\,\rho_{tip}\,a}$. The FIF is thus computed at each time step using Eq. (2) where v_{tip} in the equation is taken at previous time step.

$$\mathcal{F} \approx \frac{-1}{4\sqrt{a/d_0}(1-k)w^{ls}} \left(\int_\Gamma \nabla w^l_{PTN} \cdot \mathbf{n} \mathrm{d}\Gamma + \frac{1}{D^l} \iint_\Sigma \mathbf{v_{tip}} \cdot \nabla w^l_{PTN} \mathrm{d}\Sigma \right) \tag{2}$$

~~Values of integration parameter a are discussed in Section 3.1.~~ A first FE implementation with adaptive mesh (called PTN mesh) has been described in Ref [15]. In this implementation, a minimum mesh size h_{min} that is an order of magnitude smaller than ρ_{tip} or in the same order of magnitude as ρ_{tip} was imposed at the solid/liquid interface, and the mesh in the liquid was adapted to the solute composition gradient. This meshing strategy is efficient to compute (ρ_{tip}, v_{tip}) while limiting the number of elements in the mesh. However, it necessitates to remesh very frequently, which is numerical time consuming (see section 3.1). In this article, a new meshing strategy is proposed to limit the remeshing frequency without degrading the precision on the growth velocity.

2.1.2. Finite element metric and improved remeshing strategy

~~As for~~ Same as the first finite element implementation [15], the mesh size in the liquid far from parabolas is set to a maximum value h_{max}, because there is no need to compute the composition gradient ∇w^l_{PTN} with high resolution in this region. In addition, the mesh size in areas corresponding to the internal part of parabolas is set to a value h_{solid} (see Fig 1). As explained previously, the mesh size has to be small in the vicinity of the integration area in order to compute the FIF with a good precision. As the integration area is translated and resized at each time step with the growth of its parabolic branch, the new mesh strategy is to define a rectangular box of minimum mesh size h_{min} around the dendrite tip. This rectangle, which is defined using the orthogonal query method [17, 18], is first created at the creation of the parabola with its length aligned with the predefined parabola trajectory. Its position and dimensions (half-height H, minimum length behind the tip l_b, total box length $2l + 2l_b$, see Fig 1) are defined according to the dimensions of the integration area of the parabola at the time of creation of the box, identified by a $'cr'$ subscript in the followings. In simulations presented in Section 3, these parameters are scaled as $H = 1.5R^{cr}_{integ}$, $l_b = 1.2a^{cr}$, and $l = 10\delta^{cr}_{d_{Iv}}$ where $\delta_{d_{Iv}}$ is the diffusion length along the growth direction at stationary state.

~~In order to limit the remeshing frequency and to ensure a fine mesh in the integration area at each time step, a rectangular box is defined in front of each parabola using the orthogonal query method [17, 18]. This box, which is aligned with the predefined parabola trajectory, will be crossed by the growing branch and recreated as soon as the integration area reaches its edge. Parameters defining the dimensions and position of the box (half-height H, minimum length behind the tip l_b, total box length $2l + 2l_b$) are reported in Fig 1. These parameters are defined according to the dimensions of the integration area of the parabola at the time of creation of the box, identified by a c exponent in the followings. In simulations presented in Section 3, these parameters are scaled as $H = 1.5R^c_{integ}$, $l_b = 1.2a^c$, and $l = 10\delta_{d_{Iv}}$ where $\delta_{d_{Iv}}$ is the diffusion length along the growth direction at stationary state.~~ The definition of $\delta_{d_{Iv}}$ is given in Appendix A. ~~The mesh in this box has minimum mesh size h_{min}.~~ The rectangle will therefore be crossed by the parabolic tip and its integration area during the growth of the branch, and it will have to be displaced and resized as soon as the integration area is about to get out of it, which could happen in two situations: (i) the tip has almost crossed the whole rectangle and the integration area is at the edge of the rectangle (ii) the tip velocity has decreased, its integration area is larger and is about to exceed the height of the rectangle.

To facilitate the ~~transitional~~ transition from h_{max} to h_{min} at the creation of the box, two transition areas TA1 and TA2 of thickness e_1 and e_2 and mesh size h_1 and h_2 are defined (Fig 1). The choice of values of mesh size in the various regions of the simulation domain (h_{min}, h_{max}, h_{solid}, h_1 and h_2) is a compromise between the precision and the necessity to limit the number of elements in the simulation domain. This study will be detailed in Section 3 as part of a convergence study. This strategy permits to limit the remeshing frequency while limiting the number of elements in the simulation.

2.2. CAPTN method

This section is a recall of the CAPTN coupling and the adaptation of the CA model to this coupling [15]. Some improvements are also presented.

2.2.1. CA model adapted to the PTN coupling

The CA model aims at predicting the grain structure generated during solidification processes. This method is based on the approximation of dendritic grains as orthodiagonal quadrilaterals (resp. orthodiagonal octahedrons) in 2D (resp. in 3D) at the scale of CA cells (see Fig 2). The diagonals of the polygon are aligned with the dendrite branches. Grain growth is thus modeled by the growth of the branches which eventually capture neighboring cells by entering in their circumscribed circle (Fig 2 shows the time of capture of the blue cell by the red polygon. The green cell has been captured in a previous time). A new polygon attached to the captured cell is therefore created with the same diagonal orientation as the capturing polygon. The way the capturing polygon enters in the circumscribed circle of the captured neighboring cell permits to identify a capturing branch (S_0^μ for the green cell ν and S_2^μ for the blue cell ζ in Fig 2), which is propagated by the new polygon. This branch of the new polygon is called "principal branch" (S_0^ν for the green envelope, and S_0^ζ for the blue envelope). The branch opposite to this branch is called "opposite branch" (S_1^ν for the green envelope, and S_1^ζ for the blue envelope) and the two other branches are called "side branches" (S_2^ν and S_3^ν for the green envelope, and S_2^ζ and S_3^ζ for the blue envelope). This method of capturing cells and initializing polygons induces that a polygon center can be out of its corresponding cell. This is for example the case in Fig 2 for blue and green polygons, whereas the red polygon is a grain seed (so not created from capture), with its center locates in its corresponding cell.

2.2.2. Branches growth velocity

The principle of the CAPTN model is to compute the growth velocity of polygon branches by using the PTN method. A ~~parabola~~ paraboloid truncated by a cylinder

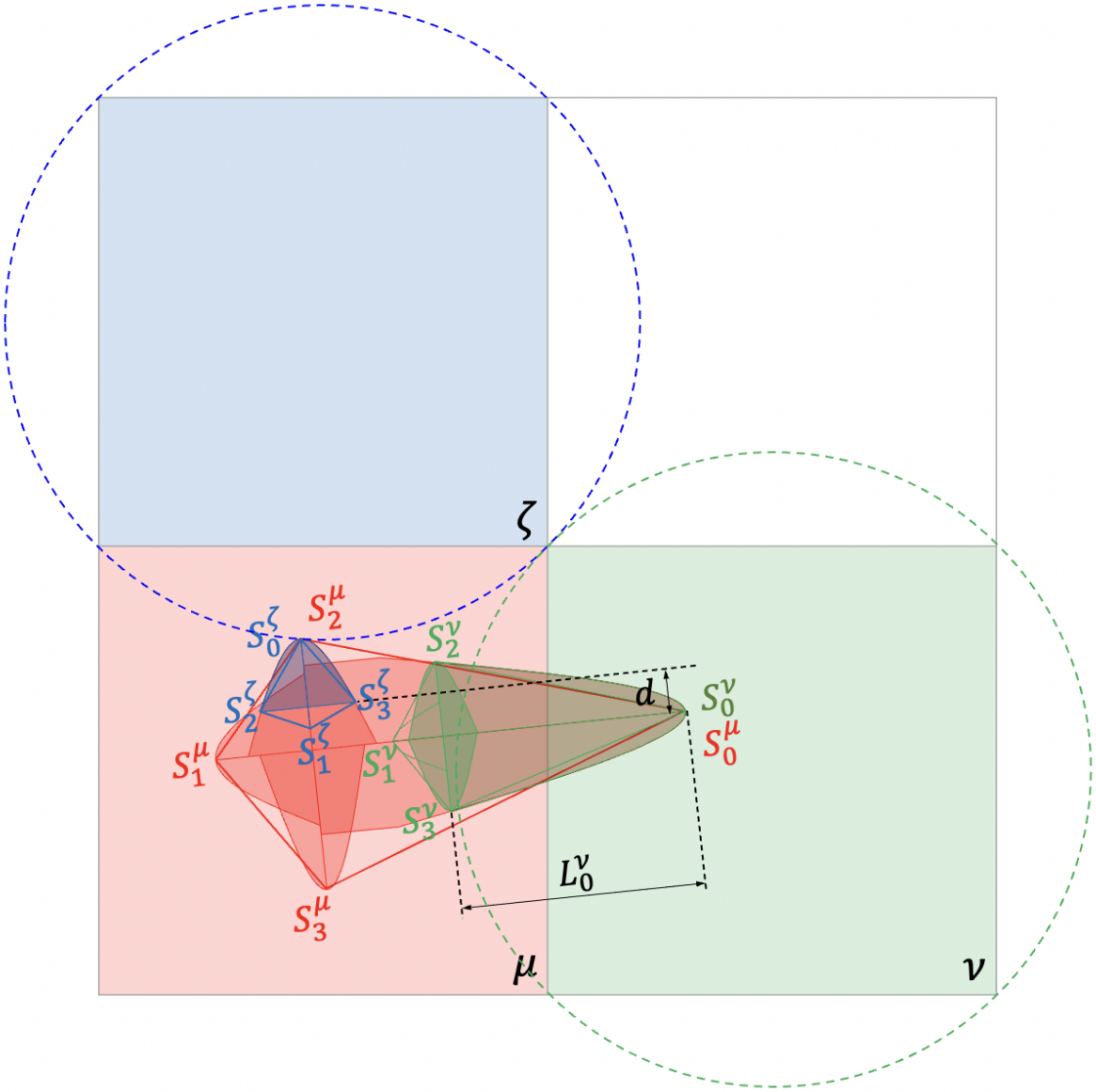

Figure 2: Process of grain propagation on the CA grid. At a previous time, the S_0^μ branch of the red polygon associated to the red cell μ ~~enters~~ has entered in the circumscribed circle of the green cell ν, leading to the creation of the green polygon. The length of the principal branch of the green polygon, S_0^ν, is denoted as L_0^ν. At the time of the image, the S_2^μ branch of the red polygon enters in the circumscribed circle of the blue cell ζ, leading to the creation of the blue polygon and the switch of the cell state from liquid to containing growing dendritic branches. The distance between the principle branch of the red polygon S_0^ν and side branch of the blue polygon S_3^ζ is defined as d. A parabola is associated to each branch except for the opposite branches (S_1^ν for the green envelope, and S_1^ζ for the blue envelope) and the eliminated side branches (S_2^ζ and S_3^ζ for the blue envelope, if $d < 2\,r_{cyl}$).

(corresponding to a parabola truncated by a rectangle in 2D) is thus defined on the PTN mesh for each branch growing on the CA grid (see Fig 2). For polygons created by the capture of a cell, the principal branch is the continuity of the already existing capturing branch. Therefore, its parabola is the same as the one of the capturing branch. Opposite branches are towards the existing branches, they can not grow, hence there is no parabola associated to the opposite branches. The initial length of side branches is limited to the thickness of the principal branch parabola. As shown in Fig 2, for the green polygon, the initial length of S_2^ν and S_3^ν are limited to the thickness of S_0^ν. In order to avoid perturbation of the growth of the principal branch due to the growth of side branches, the growth of side branches is permitted only when the length of the principal branch L_0^ν is such that $L_0^\nu > \min(3\,r_{cyl}, 2\sqrt{2}\,l_{CA})$. Their initial velocity is set to the velocity of the principal branch at this time. However, the PTN method can be applied to compute the growth velocity of a branch only if this branch is longer than the integration distance a. In this model, for security, the PTN method is used to compute the velocity of a branch if its length is greater than $1.3\,a$. Before this, its kinetics is equal to the one at last time step. Nevertheless, this methodology can lead to the creation of branches which are very close to already existing branches growing in the same direction (an example is given in Fig 2 with branches identified by the distance d). In order to avoid such non-physical events, branches at a distance lower than $2\,r_{cyl}$ from an already existing branch growing in the same direction are not allowed to grow. In Fig 2, $d < 2\,r_{cyl}$, so S_2^ζ and S_3^ζ of the blue polygon cannot grow, so they do not have associated parabolas.

When a polygon associated to a cell has captured all its neighboring cells, the polygon associated to the cell is suppressed. In this case, the PTN mesh is coarsened to a mesh size equal to h_{max}.

3. Applications

The capacity of the CAPTN model to capture physical quantities of the columnar growth of dendrites is studied. For this, the growth of dendritic grains in a constant temperature gradient $G = \boldsymbol{G} \cdot \hat{\boldsymbol{z}}$ with isotherms moving at constant velocity $v_L = \boldsymbol{v_L} \cdot \hat{\boldsymbol{z}}$ is modeled, where $\hat{\boldsymbol{z}}$ is the unit vector in the vertical direction. As the model precision depends on the choice of numerical parameters, in particular those involved in the FE implementation of the PTN model, this section starts with a study of the convergence of the PTN model to theoretical kinetics in Section 3.1. The CAPTN model is then evaluated on its ability to reproduce primary dendrite arm spacing in Section 3.2 and grain boundary

orientation angle in Section 3.3. This study is performed on a succinonitrile - 1.3wt.% acetone alloy whose properties are given in Table 1. The choice of this alloy, temperature gradient and isotherm velocity ranges is driven by comparisons of simulation results with PF and CA simulations published in previous studies in section 3.3. The influence of this choice on the precision of CAPTN results is discussed in section 3.1.

Table 1: Properties of the succinonitrile - 1.3wt.% acetone alloy

Quantity	Variable	Value	Unit	Ref
Nominal composition	w_0	1.3	wt.%	
Interdiffusion coefficient in liquid	D^l	1.270×10^{-9}	$\mathrm{m}^2 \cdot \mathrm{s}^{-1}$	[19]
Segregation coefficient	k	0.1		[19]
Liquidus slope	m	-3.02	$\mathrm{K} \cdot \mathrm{wt}\%^{-1}$	[20]
Liquidus temperature	T_L	327.314	K	[20]
Gibbs-Thomson coefficient	Γ^{ls}	6.4×10^{-5}	$\mathrm{K} \cdot \mathrm{mm}$	[21]
Selection parameter	σ	0.057		[16]

For all simulations, the initial temperature at the bottom of the simulation domain is equal to the liquidus temperature T_L (Table 1). At any time t and position z, the temperature is computed as $T(t, z) = T_L + G(z - z_0) - G \cdot v_L(t - t_0)$, with z_0 and t_0 the lowest coordinate of the simulation domain and the initial time, respectively.

3.1. Analyze of numerical parameters

As seen in Section 2.1, the FE implementation of the PTN model necessitates to calibrate numerical variables. The CAPTN model has been evaluated in a previous study [15] on this capacity to reproduce analytical solutions of the growth of a single parabolic branch in isothermal domains for supersaturation values lower than $\Omega = 0.5$. It was observed that for a same scaling of numerical parameters on theoretical microstructure scales, the errors on ρ_{tip} and v_{tip} computed compared to analytical solutions increased with supersaturation. These results are in agreement with DNN simulations [22]. It was also observed that for a given supersaturation, simulation errors decreased with a decrease of minimum mesh size and and the increase of the integration distance a. Simulations presented in Sections 3.2 and 3.3 analyse the growth of columnar dendritic grains. In theory, the steady state of an isolated dendrite tip aligned with the temperature gradient is such that its velocity is equal to v_L and its curvature radius corresponds to the solution of Eq. (1a), giving a Peclet number $\mathrm{Pe} = \rho_{\mathrm{tip}} v_L / 2D^l$. The Ivantsov solution [23] gives an analytical expression of the steady state composition in the liquid according to Pe during to the growth of an isolated parabola (see Eq. A.2). Therefore, the analytical

expression of the equilibium composition in the liquid at the solid/liquid interface is given by ~~with w^{ls} corresponding to~~ the Ivantsov solution w^{ls}_{Iv} [15]. Furthermore, as curvature undercooling is neglected, ~~In this configuration, the radius of curvature is written as $\rho_{tip_{Iv}}$ and $\Delta T_{Iv} = -m(w^{ls}_{Iv} - w_0)$.~~ the tip undercooling ΔT_{tip} should converge to the solute undercooling corresponding to w^{ls}_{Iv} ($\Delta T_{tip} = -m(w^{ls}_{Iv} - w_0)$). The curvature radius and tip undercooling corresponding to this analytical solution are respectively written $\rho_{tip_{Iv}}$ and ΔT_{Iv}.

In order to calibrate numerical parameters for simulations, a single parabolic branch is placed in a box of 20×20 mm^2. It is aligned with a temperature gradient $G = 0.475$ K $\cdot$ mm^{-1} and a constant isotherm velocity $v_L = 0.086$ mm $\cdot$ s^{-1}. In these conditions, ~~the theoretical~~ curvature radius and undercooling of the tip ~~are given in~~ should converge to the second row values in Table 2 ~~for three values of the velocity~~.

Table 2: Ivantsov solutions for different isotherm velocities using the material parameters listed in Table 1

v_L (mm $\cdot$ s^{-1})	Ω	$\rho_{tip_{Iv}}$ (mm)	$\delta_{d_{Iv}}$ (mm)	ΔT_{Iv} (K)
0.043	0.2988	2.620×10^{-3}	0.0176	1.4441
0.086	0.3386	1.805×10^{-3}	0.0099	1.7208
0.172	0.3811	1.242×10^{-3}	0.0056	2.0496

The Numerical parameters influencing the kinetics of the tip and analyzed in this section are the integration parameter a, the minimum mesh size h_{min} and the time step Δt. Other parameters are scaled using parameters given in Table 3. The integration parameter a has to be big enough to compute the solute gradient in front of the tip with a good precision. It is therefore scaled as $a = \frac{\delta_{d_{Iv}}}{\alpha}$ where α is a dimensionless constant and

$$\delta_{d_{Iv}} = 2\Omega D^l / v_L \tag{3}$$

the diffusion length along the growth direction of the ~~Ivanstov~~ Ivantsov solution. Ω is the supersaturation, defined as $\Omega = [w^{ls}_{Iv} - w_0]/[(1-k)w^{ls}_{Iv}]$. The minimum mesh size h_{min} has to be small enough to describe the parabolic branch tip and the solute composition field around the tip. Similarly, the time step Δt has to be small enough to keep track of the solute composition field. These quantities are thus scaled such that $h_{min} = \gamma\, \rho_{tip_{Iv}}$ and $\Delta t = \tau \frac{h_{min}}{v_L}$ with γ and τ being dimensionless parameters.

Fig 3 presents the average undercooling ΔT_{tip} and curvature radius ρ_{tip} computed at steady state for different values of parameters α, γ and τ. Error bars represent the

standard deviation of ΔT_{tip} and ρ_{tip} at steady state , within a timescale of 20 s = 953 $\frac{\rho_{tip_{Iv}}}{v_{tip_{Iv}}}$. These errors are due to fluctuations in the calculation of the FIF on a finite number of elements as the length of the parabolic branch increase. For each curve, other parameters are set to the value 0.5. It is observed that whereas the parameter τ has almost no influence on results, the variation of the minimum mesh size with γ has a large effect on the precision of the simulation. In this regime of α, larger integration distance leads to more precise results owing to larger domain near the tip involved in the calculation of kinetics, which agrees with the results in [15]. It is also observed that numerical parameters have a higher influence on the precision of the undercooling than on the curvature radius.

Taking the same simulation domain and parameters $\alpha = 0.5$, $\gamma = 1$ and $\tau = 1$, the simulation using the PTN mesh described in Ref [15] takes 14 hours on 8 CPU processors to displace the tip by 9.25 mm, with 2714 times of remeshing, whereas it only takes 2 hours for the same number of processors to displace it by the same distance with the new meshing strategy, with only 93 times of remeshing. The simulation time is therefore drastically reduced with the new mesh strategy.

For a balance between accuracy and the efficiency of computation, dimensionless parameters are set to $\alpha = 0.5$, $\gamma = 1.5$ and $\tau = 1$ for simulations in Sections 3.2 and 3.3. The undercooling of this selection of parameters is 1.928 K in average with standard deviation 6.551×10^{-4} K, and the curvature radius of this selection of parameters is 1.775×10^{-3} mm in average with standard deviation 2.484×10^{-5} mm. These results are the same as the results of $\alpha = 0.5$, $\gamma = 1.5$ and $\tau = 0.5$ in Fig 3, which are 1.924 K in average with standard deviation 4.972×10^{-4} K for undercooling, and 1.776×10^{-3} mm in average with standard deviation 2.624×10^{-5} mm for radius curvature. Other numerical parameters are set to values given in Table 3. It has to be observed that errors on undercooling and curvature radius computed compared to analytical solutions are related to the high supersaturation values studied in this article. The minimum value of the steady state radius of truncating cylinder is $r_{cyl}^{min} = \sqrt{2\, a\, \rho_{tip_{Iv}}}$. If the radius of truncating cylinder r_{cyl} is greater than r_{cyl}^{min}, the kinetics of the branch is not influenced by the truncation [7, 15]. Thus, in our application, r_{cyl} is fixed as $r_{cyl} = 2\, r_{cyl}^{min}$.

3.2. Primary dendritic arm spacing for a single crystal

The spacing developed between primary branches during directional growth is a complex phenomenon. Experimental studies on various alloys [20, 24, 25] have shown that for a given temperature gradient and isotherms velocity, this spacing is not unique and can vary along the solidification front, giving a λ_1 distribution limited by two values λ_1^{min} and

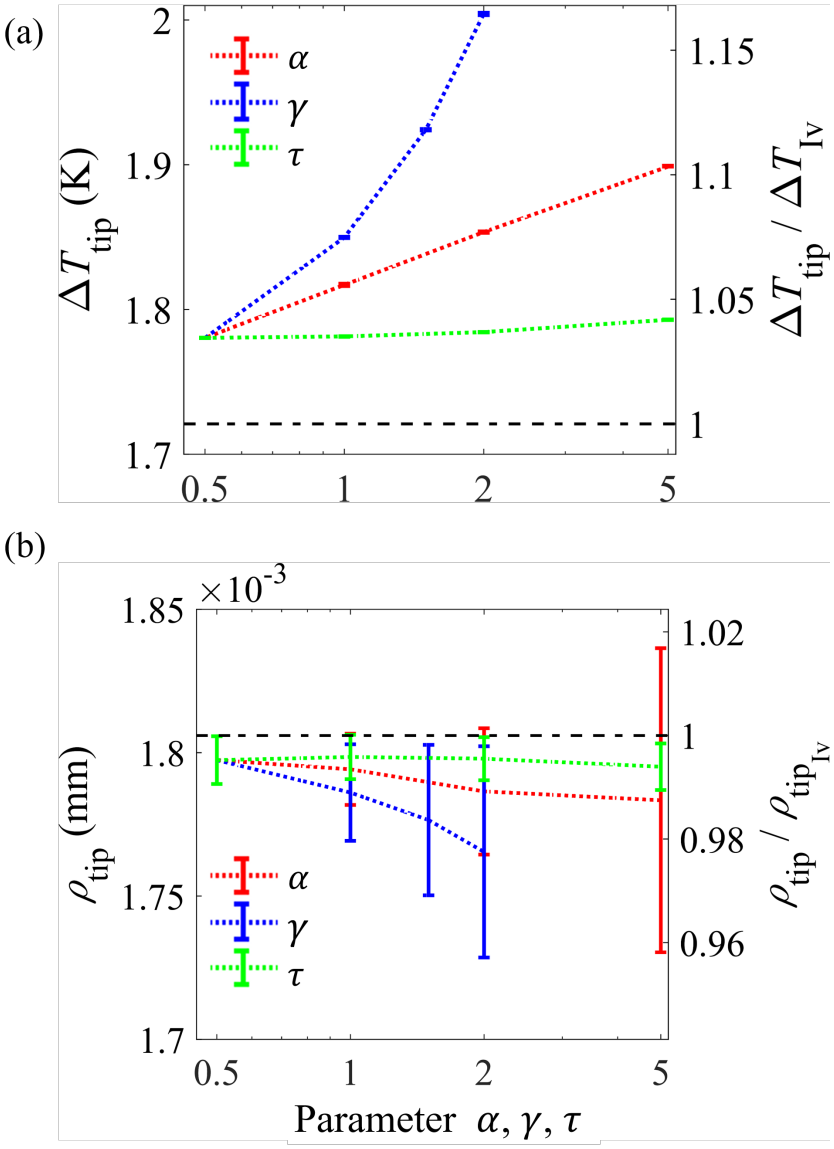

Figure 3: Evolution of steady state quantities (a) ΔT_{tip} and $\Delta T_{tip}/\Delta T_{Iv}$ and (b) $\rho_{tip_{Iv}}$ and $\rho_{tip}/\rho_{tip_{Iv}}$ according to numerical parameters (red) α, (blue) γ, and (green) τ for a single parabolic branch aligned with a constant temperature gradient $G = 0.475\ \mathrm{K \cdot mm^{-1}}$ and a constant isotherm velocity $v_L = 0.086\ \mathrm{mm \cdot s^{-1}}$. Black dashed lines correspond to Ivantsov solutions presented in Table 2. For each curve, only one parameter is varied, while the others are maintained to their minimum value, 0.5.

Table 3: Simulation parameters used in Sections 3.2 and 3.3

Variable	Name	Unit	Value
Minimum PTN mesh size	h_{min}	$\rho_{tip_{Iv}}$	1.5
PTN mesh size in TA1	h_1	h_{min}	3
PTN mesh size in TA2	h_2	h_{min}	10
PTN mesh size in solid	h_{solid}	h_{min}	10
Maximum PTN mesh size	h_{max}	h_{min}	50
Integration distance	a	$\delta_{d_{Iv}}$	2
Distance from the tip to the center of the fine mesh rectangle at its creation	l	$\delta^{cr}_{d_{Iv}}$	10
Distance from the tip to the end of the fine mesh rectangle at its creation	l_b	a^{cr}	1.2
Half height of the fine mesh rectangle	H	R^{cr}_{integ}	1.5
TA1 thickness	e_1	l	1
TA2 thickness	e_2	l	1

λ_1^{max}. This result has been retrieved in simulations using the μCA [26] and DNN methods [27]. This possible range of λ_1 values has been proved theoretically by Warren and Langer [28] who have shown that the spacing between primary branches is history dependent. Analytical studies using more restrictive assumptions [29, 30] predict that for isotherms velocities higher than a transition rate $v_{tr} = GD^l/[(1/k-1)mw_0]$, the primary spacing should evolve as $\lambda_1 \propto v_L^{-1/4} G^{-1/2}$. In experimental studies, dependencies according to $\lambda_1 \propto v_L^{-b} G^{-c}$ with scattered values of coefficients b and c have been found.

The CAPTN model is now used to demonstrate its capability to model the branching of dendrites and the solute interaction between dendrite branches, hence yielding a stable selection of the primary dendrite arm spacing during directional growth. To analyze this, a single seed with 5 μm branch length aligned with the temperature gradient is placed at the bottom center of a box of 10×17 mm^2 in width and height. During the simulation, the grain captures neighboring CA cells and propagates on the whole width of the domain, forming a network of dendrite branches which then grow vertically, leading to a selection of primary branches. An example of the dendrite network generated during a CAPTN simulation is presented in Fig 4. The spreading of the grain on the simulation domain through secondary branches can clearly be observed on the bottom part of the domain. Elimination and creation of tertiary branches can also be spotted during grain growth.

Fig 5 shows the solidification front at $t = 135$ s for the same simulation. CA cells containing a growing polygon, i.e., with at least one liquid neighboring cell, are presented as white empty squares and the solute composition field is presented as wireframe on the PTN mesh. The area with fine mesh defined in Section 2.1 can be observed in front of each parabolic tip with a liquid composition close to the alloy nominal composition (in blue). Inside branches, the composition is imposed by the Dirichlet condition to the

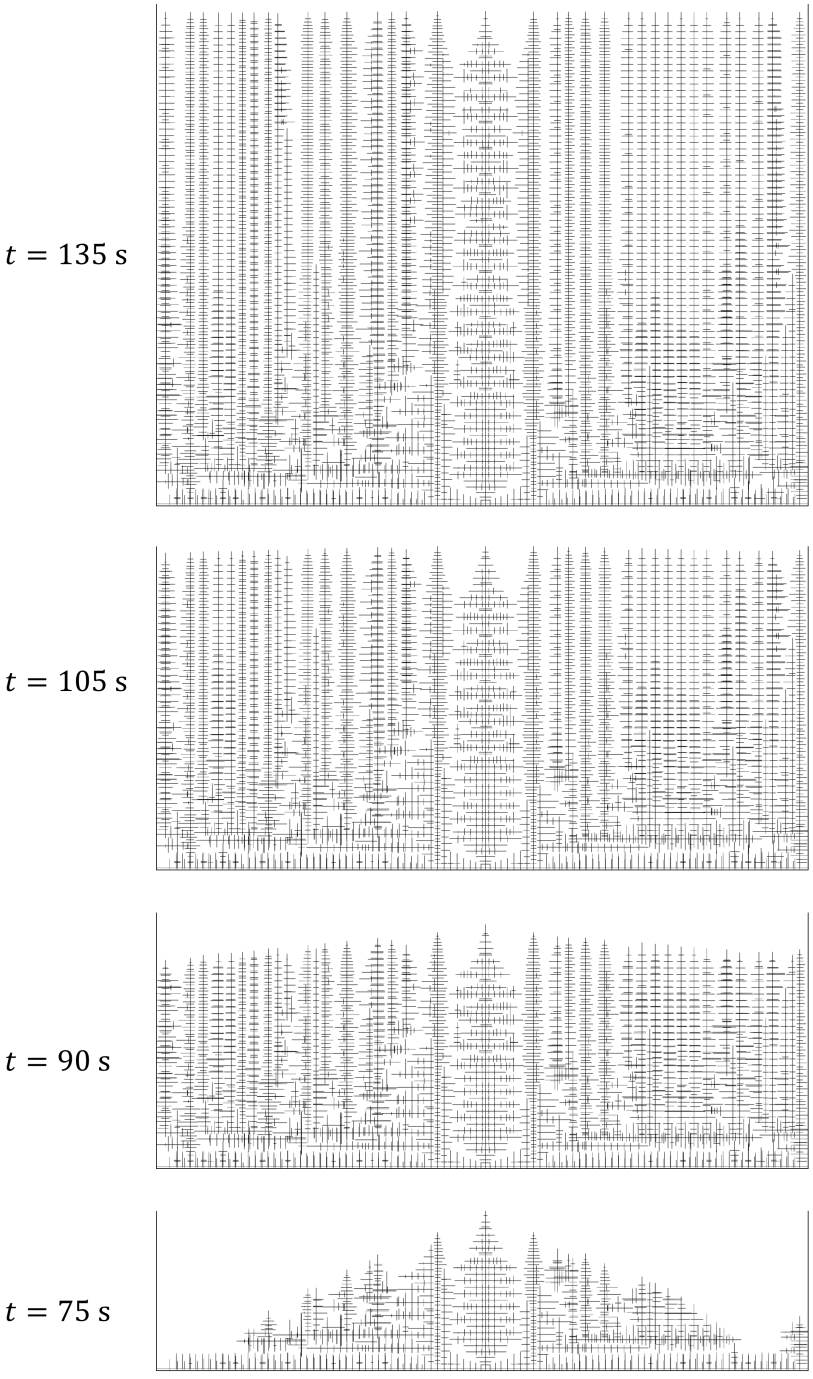

Figure 4: Dendrite needle network at different times ($t = 75\,\mathrm{s}$, $t = 90\,\mathrm{s}$, $t = 105\,\mathrm{s}$, and $t = 135\,\mathrm{s}$) in a CAPTN simulation for $G = 0.475\ \mathrm{K \cdot mm^{-1}}$, $v_L = 0.086\ \mathrm{mm \cdot s^{-1}}$ and $l_{CA} = 0.1$ mm. The domain width is 10 mm.

liquidus composition corresponding to the local temperature. One can also observe the coarse mesh on the lower part of the image, as CA cells are deallocated.

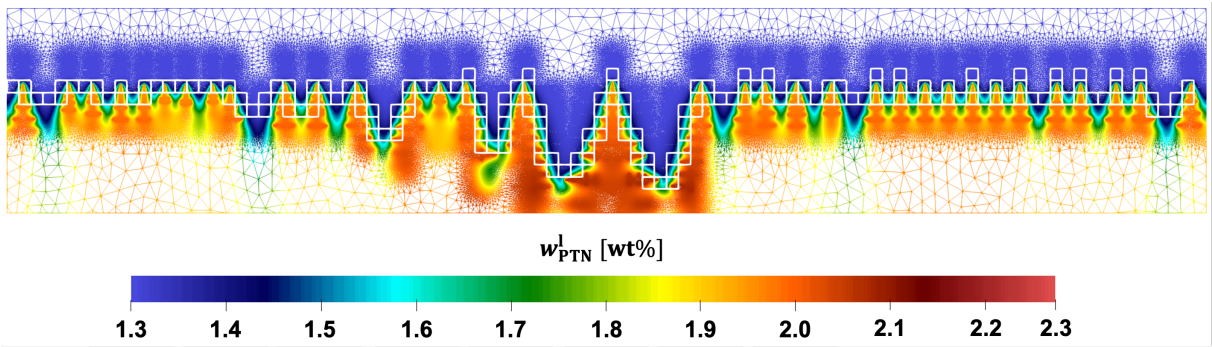

Figure 5: Wireframe of solute composition field in the liquid phase at the solidification front at $t = 135$ s in a CAPTN simulation for $G = 0.475\ \mathrm{K \cdot mm^{-1}}$, $v_L = 0.086\ \mathrm{mm \cdot s^{-1}}$ and $l_{CA} = 0.1$ mm. CA cells containing a growing polygon are represented as white squares. The domain width is 10 mm.

To measure primary dendrite arm spacing in simulations, a thickness δy of the solidification front is defined from the position of the highest primary branch. This thickness is taken as $\delta y = 1/2\bar{\lambda_1}$, where $\bar{\lambda_1}$ is the average value of λ_1 measured in the simulation. The spacing between branches with tip aligned with the gradient located in this thickness is then measured. This measurement is recursive until the $\bar{\lambda_1}$ used for δy is the same as the $\bar{\lambda_1}$ measured at this time. Fig 6 (a) shows the distribution of measured λ_1 for various cell size and Fig 7 (a) shows the evolution of the average λ_1, and of the maximum and minimum value of λ_1 with l_{CA} for $G = 0.475\ \mathrm{K \cdot mm^{-1}}$ and $v_L = 0.086\ \mathrm{mm \cdot s^{-1}}$. It can be observed on Figures 4 and 5 for $l_{CA} = 0.1$ mm that the primary spacing around the central branch corresponding to the initial position of the seed is quite large. This spacing is the highest measured value in Fig 6 (a). This large spacing can be related to the solute distribution around secondary branches in Fig 5 at the beginning of the simulation preventing the growth of tertiary branches and so limiting the filling by new tertiary branches. Furthermore, the spacing between primary branches far from the center of the simulation domain (edge branches set apart) is quite small and close to $\lambda_1 \approx 0.2$ mm. These side areas have similar histories with almost no elimination of branches during growth.

It is observed in Fig 6 (a) and Fig 7 (a) that the distribution of λ_1 converges toward a distribution with an average value $\bar{\lambda_1}$ around 0.26 mm with the decrease of cell size. As explained in section 2.2, in the CAPTN model, the spacing between tertiary branches of a given grain depends on the process of cell caption by neighbor cells polygons and

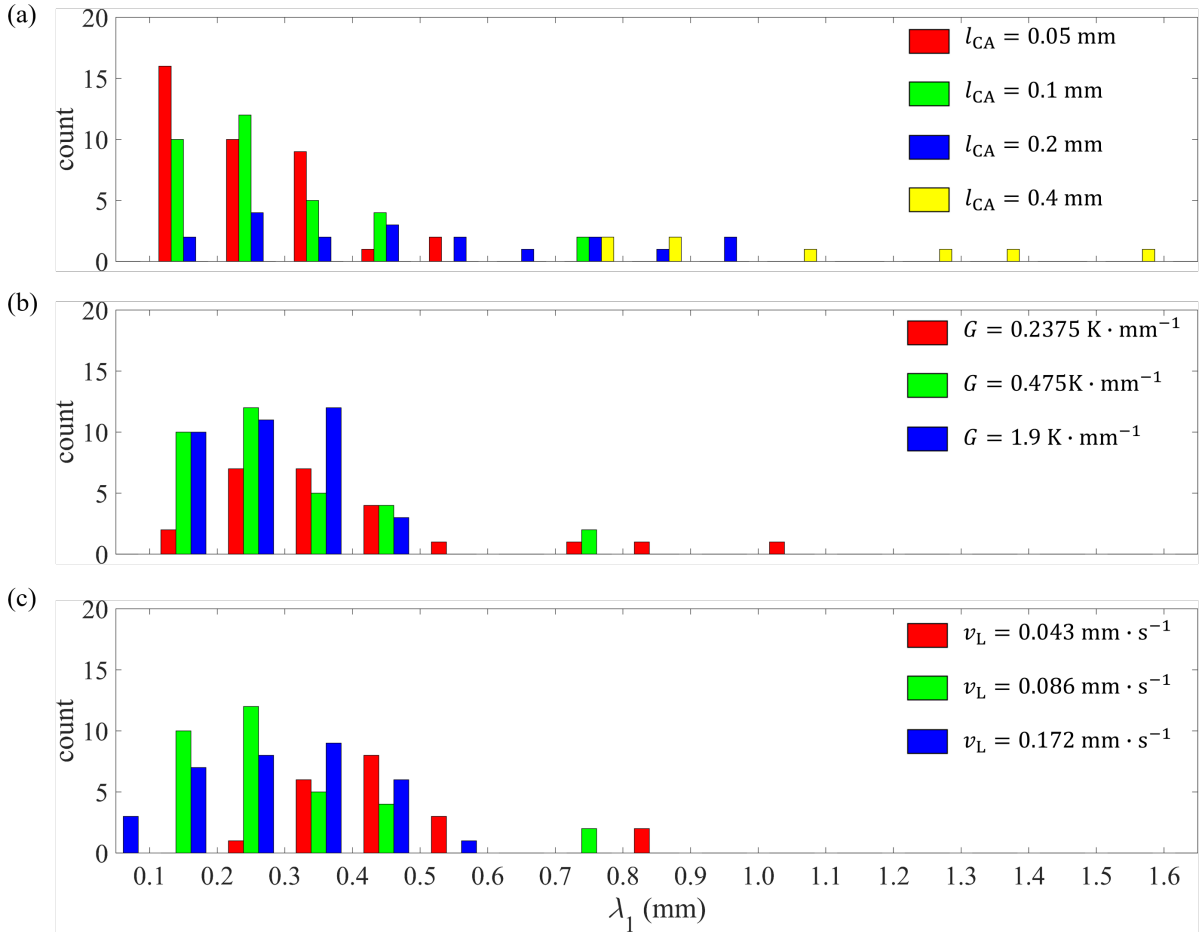

Figure 6: Distribution of λ_1 according to (a) cell size for $G = 0.475$ K · mm^{-1} and $v_L = 0.086$ mm · s^{-1}, (b) temperature gradient for $l_{CA} = 0.1$ mm and $v_L = 0.086$ mm · s^{-1} (c) isotherm velocity for $l_{CA} = 0.1$ mm and $G = 0.475$ K · mm^{-1}

thus, on the distance to grow for a branch to reach the circumscribed circle of a neighbor cell. Therefore, as there can be only one polygon associated to a given cell, in average, the distance between tertiary branches can not be lower than l_{CA}. ~~As this value is lower than 0.4 mm,~~ It seems therefore logical that the simulation using $l_{CA} = 0.4$ mm is not capable to predict ~~this~~ the converged average spacing as the spacing between branches is artificially constrained to a higher value with this parameter value.

Figures 6 (b) and (c) show the evolution of the distribution of λ_1 with the temperature gradient and isotherm velocity respectively. In addition, Figures 7 (b) and (c) present the evolution of λ_1^{min}, $\bar{\lambda_1}$ and λ_1^{max} according to these two values. These studies use a CA cell size $l_{CA} = 0.1$ mm.

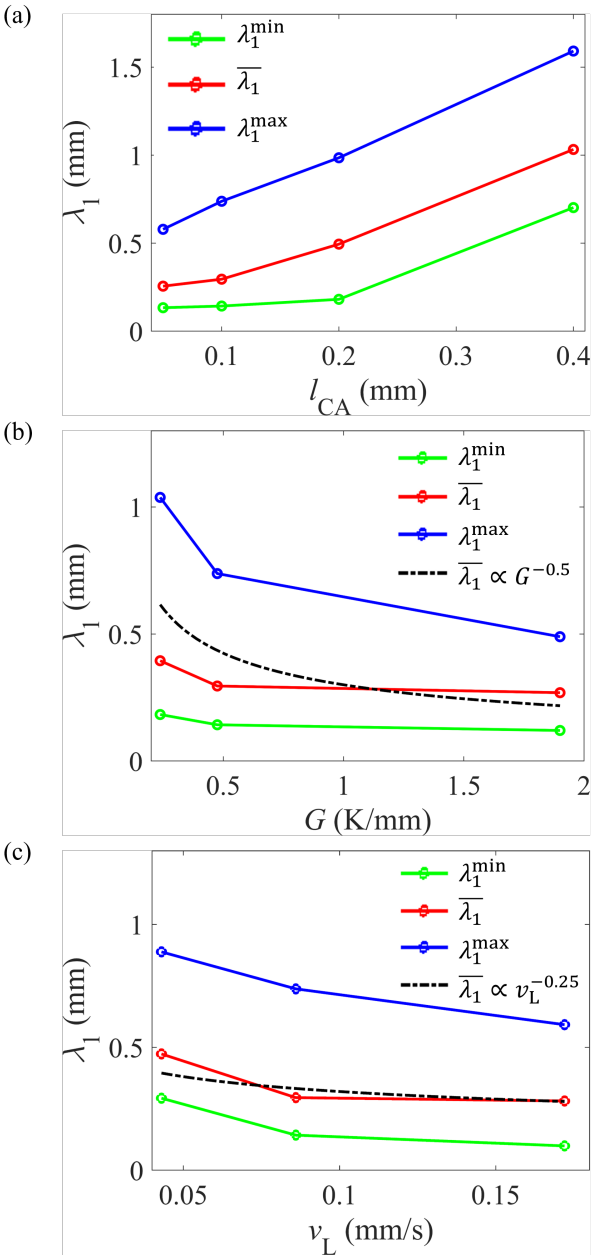

Figure 7: λ_1^{min}, $\bar{\lambda_1}$ and λ_1^{max} according to (a) cell size for $G = 0.475$ K $\cdot$ mm^{-1} and $v_L = 0.086$ mm $\cdot$ s^{-1}, (b) temperature gradient for $l_{CA} = 0.1$ mm and $v_L = 0.086$ mm $\cdot$ s^{-1} (c) isotherm velocity for $l_{CA} = 0.1$ mm and $G = 0.475$ K $\cdot$ mm^{-1}. Black lines are theoretical laws with $G^{-0.5}$ (b) and $v_L^{-1/4}$ (c) dependencies fitted on $\bar{\lambda_1}$ simulation values.

It can be observed that the average value of λ_1 tends to decrease with both G and v_L. Moreover, theoretical laws proportional to $G^{-1/2}$ and $v_L^{-1/4}$ are respectively reported in Figures 7 (b) and (c). It can be observed that whereas the $v_L^{-1/4}$ dependency fits quite well the evolution of $\bar{\lambda_1}$ with v_L, the $G^{-1/2}$ dependency seems to overestimate the variation of $\bar{\lambda_1}$ with the temperature gradient. It is also observed that the variation of temperature gradient has a stronger effect on the range of λ_1 values compared to the velocity, with an enhanced gap between λ_1^{max} and λ_1^{min} at low G compared to high G.

3.3. Diverging grain boundary orientation angle for a bi-crystal

The inclination of the grain boundary between two grains with different inclinations growing in a constant temperature gradient G with a constant isotherm velocity v_L has been studied using PF and CA methods [31, 16, 32, 33, 34]. It has been shown that the value of the angle of the grain boundary is contained between two theoretical limits: the Favorably Oriented Grain (FOG) [16, 34, 35] and the Geometrical Limit (GL) [16, 34]. The angle θ_D of the grain boundary formed by the diverging primary directions of two grains with inclinations $\alpha_1 = 30°$ for the left grain and $\alpha_2 = 10°$ for the right grain with the direction of temperature gradient has been analyzed in more details using PF and CA simulations [16]. In Fig 8 the blue line corresponds to the value given by the GL model and the red line corresponds to the value given by the FOG model. The central line of Figures 8 (West, Center and East) present the diverging grain boundary angle obtained with these two numerical methods as a function of the CA cell size and for $v_L = 0.086$ mm $\cdot$ s^{-1} and three values of the temperature gradient: (West) $G = 0.2375$ K $\cdot$ mm^{-1}, (Center) $G = 0.475$ K $\cdot$ mm^{-1}, and (East) $G = 1.9$ K $\cdot$ mm^{-1}. The angle given by the PF method (dashed line) is constant, with a reported variation only for the center configuration (gray window), $G = 0.475$ K $\cdot$ mm^{-1}. The angle given by the CA model (purple dots) varies continuously from the GL to the FOG value as cell size increases. This result has been explained by the fact that angle θ_D is linked to the secondary dendrite arm spacing preceding tertiary branching forming the grain boundary $\bar{\Lambda}$ indicated by orange dashed lines in Fig 8. Therefore, whereas this distance is correctly reproduced in PF simulations, it is cell size dependant in CA simulations, and values given by CA simulations are equal to the ones obtained with PF simulations if the cell size is equal to this physical spacing.

Simulations are reproduced using the CAPTN model. For this, two seeds with 5 μm initial branch length are placed at the bottom of a rectangular domain, the [1 0] branch of the left one (resp. right one) making an angle $\alpha_1 = 30°$ with the temperature gradient (resp. $\alpha_2 = 10°$). Fig 9 shows the solidification front at a given time for

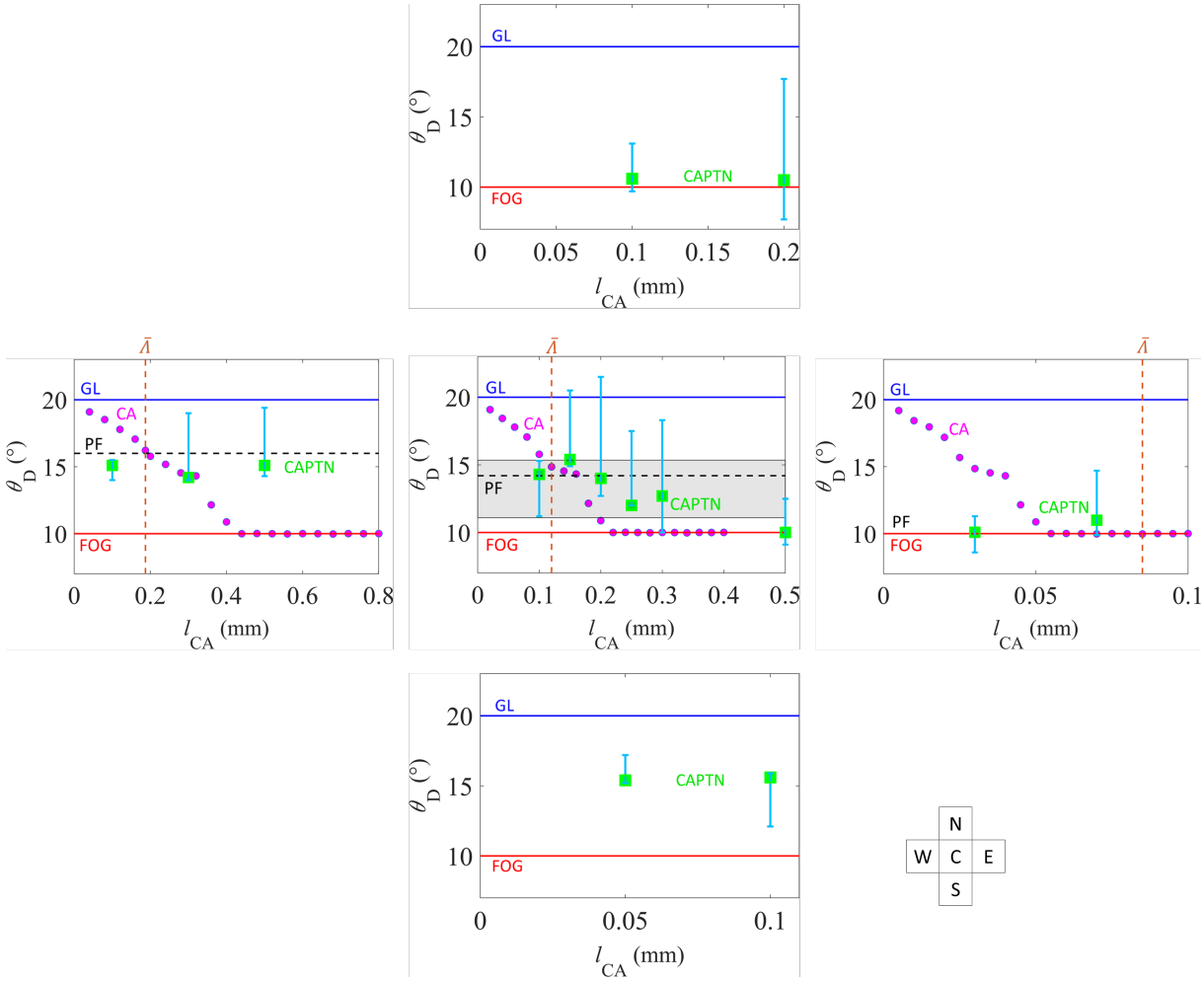

Figure 8: Evolution of the diverging grain boundary orientation angle θ_D according to l_{CA}. The blue and red lines are respectively the GL and the FOG models. Results of CAPTN simulations are presented as green squares with error bars corresponding to measurements of $\theta_{D_{min}}$ and $\theta_{D_{max}}$ presented in Fig 10. ~~and~~ CA results [16] are presented as purple circles. The black dashed line is the phase field result, with variations reported as a gray zone [16]. The dashed orange line corresponds to the secondary dendrite arm spacing preceding tertiary branching. (Center) $G = 0.475$ K $\cdot$ mm^{-1} and $v_L = 0.086$ mm $\cdot$ s^{-1} (West) $G = 0.2375$ K $\cdot$ mm^{-1} and $v_L = 0.086$ mm $\cdot$ s^{-1} (East) $G = 1.9$ K $\cdot$ mm^{-1} and $v_L = 0.086$ mm $\cdot$ s^{-1} (North) $G = 0.475$ K $\cdot$ mm^{-1} and $v_L = 0.043$ mm $\cdot$ s^{-1} (South) $G = 0.475$ K $\cdot$ mm^{-1} and $v_L = 0.172$ mm $\cdot$ s^{-1}.

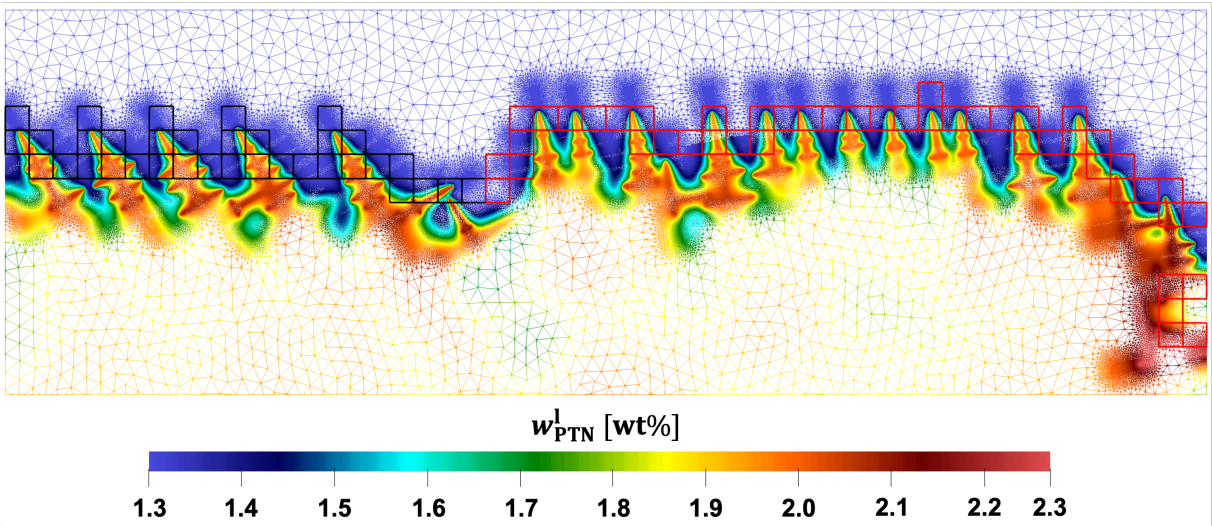

Figure 9: Wireframe of solute composition field in the liquid phase at the solidification front $t = 300$ s for the bi-crystal CAPTN simulation with $G = 0.475$ K $\cdot$ mm^{-1}, $v_L = 0.086$ mm $\cdot$ s^{-1} and $l_{CA} = 0.2$ mm. CA cells containing a growing polygon are represented as black squares for the left grain and red squares for the right grain. The domain width is 10 mm.

$G = 0.475$ K $\cdot$ mm^{-1}, $v_L = 0.086$ mm $\cdot$ s^{-1} and a cell size $l_{CA} = 0.2$ mm. The solute composition field in the liquid is presented as wireframe on the PTN mesh. As for Fig 5, a rectangular zone with fine mesh can be observed in front of each parabolic tip with an inclination corresponding to the growth direction of the tip. A coarser mesh is observed in the liquid located far from the solidification front and in the area where cells have been deallocated, i.e., with no remaining liquid neighboring cell. CA cells containing a growing polygon appear as black squares for the left grain and red squares for the right grain.

Fig 10 shows the needle network formed at the end of this simulation (a) and the corresponding cell structure (b). Black (resp. red) lines and cells are associated to the left grain (resp. right grain). The distance between highest tips of the two grains is noted δ. This distance increases at the beginning of the simulation to reach a steady state value δ_{st} (see Fig 10 (a)). The evolution of this distance is theoretically computed using velocities given by the Ivantsov growth law described in Section 3.1. It is obtained that the δ value reaches $99\%\delta_{st}$ at $t_{st} \approx 100$ s. The position of the solidification front at t_{st} is indicated as a horizontal orange dot line in Fig 10 and is located at a distance d_{st} from the bottom of the simulation domain. The angle of inclination between the grain boundary and the temperature gradient, θ_D, is measured by the inclination of the line between the position of the interface at d_{st} and at the end of the simulation (green dashed line on Fig 10). Two extreme angles are also measured for interfaces located above $2\,d_{st}$ (see the cyan

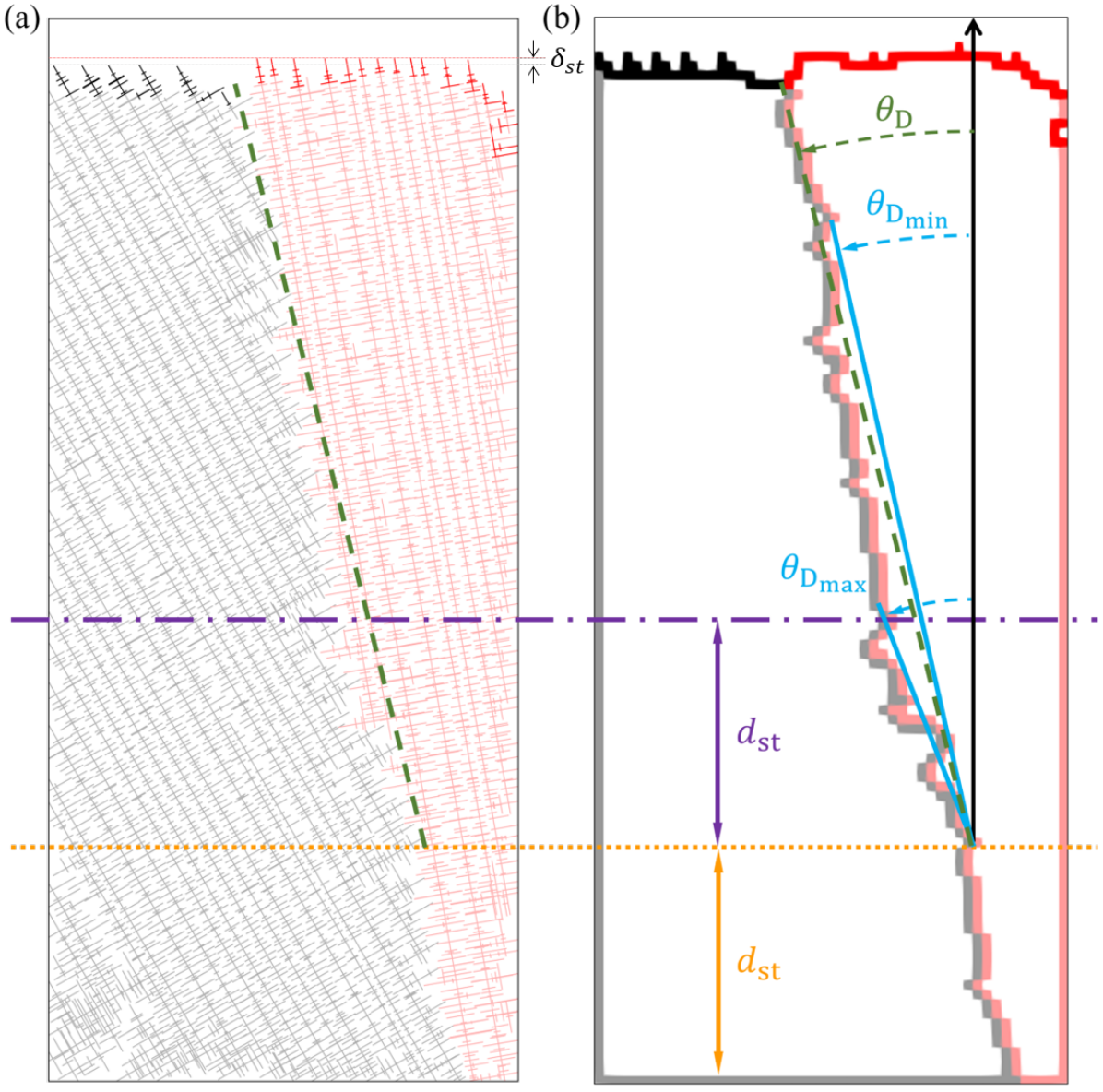

Figure 10: (a) Needle Network and (b) cell structure at the end of the CAPTN simulation $t = 300$ s for $G = 0.475\ \mathrm{K \cdot mm^{-1}}$, $v_L = 0.086\ \mathrm{mm \cdot s^{-1}}$ and $l_{CA} = 0.2$ mm. The width of the domain is 10 mm. The black color is associated to the left grain and the red color to the right grain. The CA cells containing a growing polygon, drawn in Fig 9, are represented in full opacity, and other CA cells at the grain and domain boundaries are represented in lower opacity. The white area contained within the contour defined by the black (resp. red) cell belong to the left (resp. right) grain, while the white area at the top of the domain is liquid. In (a), the branches belonging to the CA cells containing a growing polygon are drawn in full opacity, and other branches are drawn in lower opacity.

lines on Fig 10).

Angles measured with the CAPTN method as a function of the CA cell size and for various couples (G, v_L) are reported in Fig 8 as green squares. In Fig 8 Center, it is observed that, contrary to CA simulations, the angle θ_D computed with the CAPTN model is not dependent on cell size, even for l_{CA} much higher than the one corresponding to the secondary dendrite arm spacing preceding tertiary branching. It is however observed that if cell size is too large to correctly reproduce solute interactions between branches, the CAPTN model retrieves the FOG limit (see Fig 8 Center). For cell size lower than this upper limit, values obtained are in good agreement with the one of the PF method no matter the value of l_{CA}. This result indicates that the CAPTN model reproduces the $\bar{\Lambda}$ spacing, even for CA cell values much higher than this spacing. The minimum and maximum values of θ_D for a cell size lower than the $\bar{\Lambda}$ spacing are in excellent agreement with the range of values predicted by the PF simulations as they coincide with the range of the gray window. In addition, both models predict a decrease of θ_D as the temperature gradient increases for $v_L = 0.086$ mm $\cdot$ s^{-1}. This is verified in Fig 8 West, Center, and East. CAPTN simulations also predict an increase of θ_D as the isotherm velocity increases, as shown in Fig 8 North, Center, and South. These two tendencies lead to the profile of θ_D according to G/v_L displayed in Fig 11 (a) where the average θ_D value decreases from $\theta_D \simeq 15°$ at low G/v_L values to reach the FOG limit at $G/v_L \simeq 10$ K $\cdot$ s $\cdot$ mm^{-2}. The relation between θ_D and G/v_L can be approximated as

$$\frac{\theta_D - \theta_{FOG}}{\theta_{GL} - \theta_{FOG}} \propto \exp(-\beta \frac{G}{v_L}) \tag{4}$$

where θ_{GL} and θ_{FOG} are the GL and FOG limits, respectively, and $\beta > 0$. The value $\beta = 0.183$ is used in Fig 11 (a).

The step between stationary primary dendrite tips of two grains at steady state, δ_{st}, was identified as a main parameter for the control of the grain boundary orientation in Ref [34]. However, it can be observed on Fig 11 (a) that two identical values of G/v_L give similar values of θ_D but different values of δ_{st} (see Fig 11 (b)). Therefore, it seems that θ_D is a function of G/v_L rather than an function of δ_{st}, explaining the form chosen for Eq. 4. Possible relations between θ_D and $\bar{\Lambda}$ should be the topic of further investigations, following the findings reported in Ref [16].

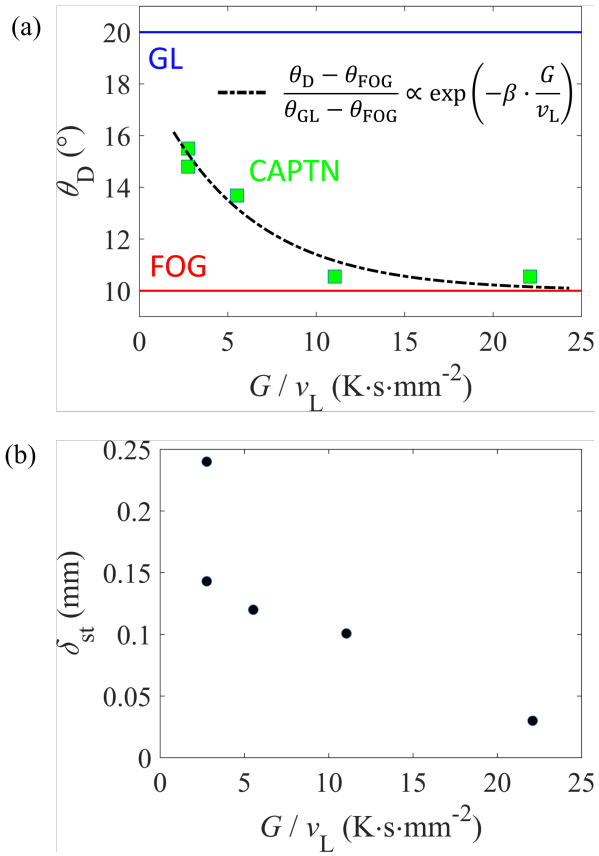

Figure 11: Evolution of (a) θ_D computed in CAPTN simulations and (b) δ_{st} computed by the Ivantsov growth law with G/v_L. In (a), the GL and FOG limits are indicated as blue and red lines respectively. The trend of θ_D is fitted by the mathematical formula $(\theta_D - \theta_{FOG})/(\theta_{GL} - \theta_{FOG}) \propto \exp(-\beta\, G/v_L)$, where θ_{GL} and θ_{FOG} are the GL and FOG limits, respectively, and $\beta > 0$.

4. Conclusions

This article presents advances on the CAPTN model which couples the cellular automation (CA) and the Parabolic Thick Needle (PTN) methods. Optimizations on the meshing strategy are presented which permit to reduce drastically computation time. A numerical parametric study is performed which shows that the model converges toward theoretical growth solutions as the ~~thinness~~ fineness of the mesh and the size of the integration area are increased. This optimized CAPTN model is then evaluated on its ability to reproduce two physical quantities developed during directional growth in a constant temperature gradient G with a constant isotherm velocity v_L: the primary dendrite arm spacing λ_1 and the diverging grain boundary orientation angle θ_D between two grains of different orientations. The grain selection between primary branches and creation of new branches from secondary and tertiary branches is well simulated as long as cell size is

sufficiently small to model solute interactions between branches. In these conditions, simulations converge toward a distribution of primary branches which depends on the history of dendrite branches. This result is in agreement with the theory of Warren and Langer [28] and experimental results. ~~Gradient and velocity dependencies on average values of these distributions have been compared with Hunt [29] and Kurz-Fisher [30] theories and are coherent with G^{-b} and v_L^{-c} power laws~~ Average primary spacings obtained tend to decrease with G and v_L, in agreement with Hunt [29] and Kurz-Fisher [30] theories. The study on the grain boundary orientation angle has revealed that, contrary to the classical CA model, the angle obtained in CAPTN simulations does not depend on cell size for a large range of cell size. This angle has been computed for various gradients and isotherm velocities and is in good agreement with previous phase field studies [16]. Moreover, the diverging grain boundary orientation angle is found to be a monotonously decreasing function of the ratio G/v_L, and the trend can be expressed by an exponential law. This article shows therefore the relevance of the CAPTN model to predict dendrite structures and competition between branches due to solute interactions. This model is now to be extended in 3D for comparisons with experimental studies.

Acknowledgments

This work was conducted within the ESA-MAP program 'CETSOL', contract 14313/01/NL/SH.

Data availability

Data will be made available on request.

Appendices

A. Diffusion length

A parabola of radius ρ_{tip} and velocity v_{tip} moves at steady state in the x direction in an infinite 2D domain. Cartesian (x, y) coordinates are defined in Fig 12 along with (ξ, η) parabolic coordinates.

The relations between these two systems of coordinates is the following:

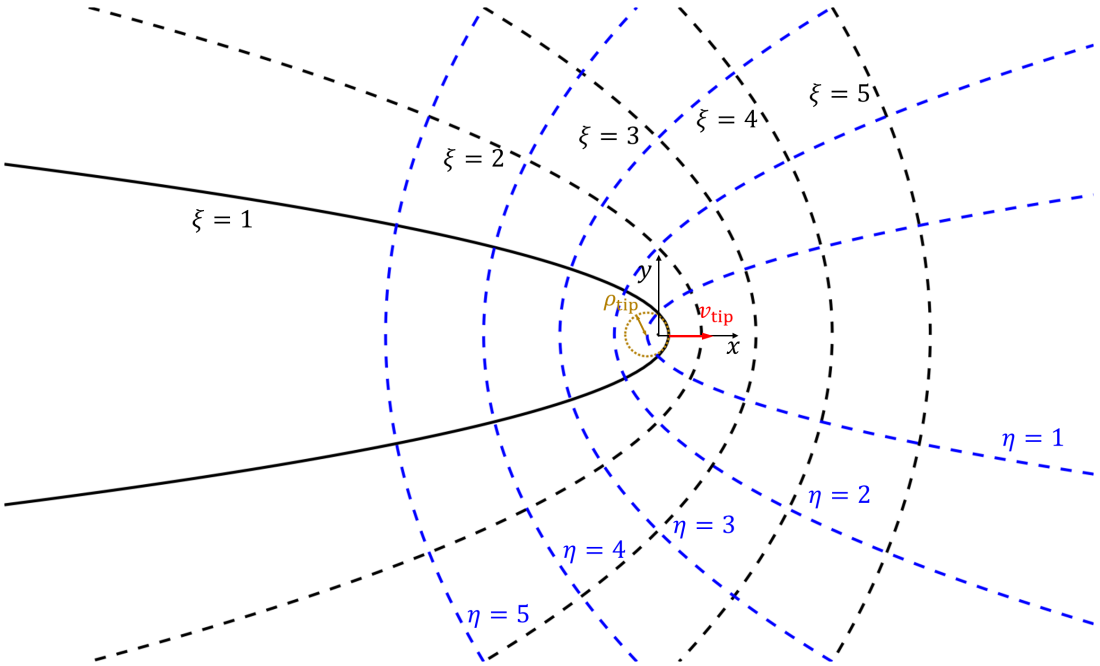

Figure 12: Parabolic and Cartesian coordinates used for the calculation of the diffusion length

$$\begin{array}{lll} \text{Parabolic} & \rho_{\text{tip}}\xi^2 = x + \sqrt{x^2+y^2} & \rho_{\text{tip}}\eta^2 = -x + \sqrt{x^2+y^2} \\ \text{Cartesian} & x = \frac{\rho_{\text{tip}}}{2}\left(\xi^2 - \eta^2\right) & y = \rho_{\text{tip}}\xi\eta \end{array} \tag{A.1}$$

In these steady state conditions, the composition field in the liquid is given by the Ivantsov solution [23]:

$$w^{\text{l}}(\xi) = w_0 + (1-k)w^{\text{ls}}\sqrt{\pi\,\text{Pe}}\cdot \text{e}^{\text{Pe}}\cdot \text{erfc}(\xi\sqrt{\text{Pe}}) \tag{A.2}$$

with $\text{Pe} = \rho_{\text{tip}} v_{\text{tip}}/2D^l$.

The diffusion length at the dendrite tip along its growing direction is defined as twice the intersection of the tangent of the composition along the x axis at the solid/liquid interface and the nominal composition w_0. From Eq. (A.2), the expression of the composition field on the x axis is derived:

$$w^{\text{l}}(x) = w_0 + (1-k)w^{\text{ls}}\sqrt{\pi\text{Pe}}\cdot \text{e}^{\text{Pe}}\cdot \text{erfc}(\sqrt{\text{Pe}\cdot 2x/\rho_{\text{tip}}}) \tag{A.3}$$

From Eq. (A.3), it is deduced that:

$$\left.\frac{\text{d}w^l}{\text{d}x}\right|_{x=\frac{\rho_{\text{tip}}}{2}} = -2(1-k)w^{\text{ls}}\,\text{Pe}/\rho_{\text{tip}} \tag{A.4}$$

Therefore, the diffusion length becomes

$$\delta_{\mathrm{d_{Iv}}} = \frac{w_0 - w^{\mathrm{ls}}}{-(1-k)w^{\mathrm{ls}}\,\mathrm{Pe}/\rho_{\mathrm{tip}}} \tag{A.5}$$

using the definition of the supersaturation Ω given in section 3.1, we obtain

$$\delta_{\mathrm{d_{Iv}}} = \frac{2\,\Omega\,D^{\mathrm{l}}}{v_{\mathrm{tip}}} \tag{A.6}$$

References

[1] W. Kurz, M. Rappaz, and R. Trivedi. Progress in modelling solidification microstructures in metals and alloys. part II: dendrites from 2001 to 2018. *International Materials Reviews*, 66(1):30–76, 2021.

[2] Zhijun Wang, Junjie Li, Jincheng Wang, and Yaohe Zhou. Phase field modeling the selection mechanism of primary dendritic spacing in directional solidification. *Acta Materialia*, 60(5):1957–1964, 2012.

[3] Toshio Suzuki, Machiko Ode, Seong Gyoon Kim, and Won Tae Kim. Phase-field model of dendritic growth. *Journal of Crystal Growth*, 237:125–131, 2002.

[4] Damien Tourret and Alain Karma. Growth competition of columnar dendritic grains: A phase-field study. *Acta Materialia*, 82:64–83, 2015.

[5] B Bellon, AK Boukellal, T Isensee, OM Wellborn, KP Trumble, MJM Krane, MS Titus, D Tourret, and J Llorca. Multiscale prediction of microstructure length scales in metallic alloy casting. *Acta Materialia*, 207:116686, 2021.

[6] D. Tourret and A. Karma. Multiscale dendritic needle network model of alloy solidification. *Acta materialia*, 61(17):6474–6491, 2013.

[7] D. Tourret and A. Karma. Three-dimensional dendritic needle network model for alloy solidification. *Acta Materialia*, 120:240–254, 2016.

[8] D. Tourret, M. M. Francois, and A. J. Clarke. Multiscale dendritic needle network model of alloy solidification with fluid flow. *Computational Materials Science*, 162:206–227, 2019.

[9] C.-H. Chen, A. M. Tabrizi, P.-A. Geslin, and A. Karma. Dendritic needle network modeling of the columnar-to-equiaxed transition. part II: three dimensional formulation, implementation and comparison with experiments. *Acta Materialia*, 202:463–477, 2021.

[10] Cheng Gu, Colin D Ridgeway, and Alan A Luo. Examination of dendritic growth during solidification of ternary alloys via a novel quantitative 3d cellular automaton model. *Metallurgical and Materials Transactions B*, 50:123–135, 2019.

[11] Cheng Gu, Colin D Ridgeway, Michael P Moodispaw, and Alan A Luo. Multi-component numerical simulation and experimental study of dendritic growth during solidification processing. *Journal of Materials Processing Technology*, 286:116829, 2020.

[12] Ch.-A. Gandin, J.-L. Desbiolles, M. Rappaz, and P. Thevoz. A three-dimensional cellular

automation-finite element model for the prediction of solidification grain structures. *Metallurgical and Materials Transactions A*, 30(12):3153–3165, 1999.

[13] T. Carozzani, H. Digonnet, and Ch.-A. Gandin. 3d cafe modeling of grain structures: Application to primary dendritic and secondary eutectic solidification. *Modeling and simulation in materials science and engineering*, 20(1):015010, 2012.

[14] Dong Rong Liu, Nathalie Mangelinck-Noël, Ch-A Gandin, Gerhard Zimmermann, Laszlo Sturz, Henri Nguyen-Thi, and Bernard Billia. Simulation of directional solidification of refined al–7 wt.% si alloys–comparison with benchmark microgravity experiments. *Acta Materialia*, 93:24–37, 2015.

[15] R. Fleurisson, O. Senninger, G. Guillemot, and Ch.-A. Gandin. Hybrid cellular automaton-parabolic thick needle model for equiaxed dendritic solidification. *Journal of Materials Science & Technology*, 2022.

[16] E. Dorari, K. Ji, G. Guillemot, Ch.-A. Gandin, and A. Karma. Growth competition between columnar dendritic grains–the role of microstructural length scales. *Acta Materialia*, 223:117395, 2022.

[17] M. Berg, M. Kreveld, M. Overmars, and O. Schwarzkopf. Computational geometry. In *Computational geometry*, pages 1–17. Springer, 1997.

[18] D. Meagher. Geometric modeling using octree encoding. *Computer graphics and image processing*, 19(2):129–147, 1982.

[19] M.A. Chopra, M.E. Glicksman, and N.B. Singh. Dendritic solidification in binary alloys. *Metallurgical Transactions A*, 19(12):3087–3096, 1988.

[20] K. Somboonsuk, J.T. Mason, and R. Trivedi. Interdendritic spacing: part i. experimental studies. *Metallurgical and Materials Transactions A*, 15(6):967–975, 1984.

[21] H. Esaka. Dendrite growth and spacing in succinonitrile-acetone alloys. Technical report, EPFL, 1986.

[22] Damien Tourret, Laszlo Sturz, Alexandre Viardin, and Miha Založnik. Comparing mesoscopic models for dendritic growth. In *IOP Conference Series: Materials Science and Engineering*, volume 861, page 012002. IOP Publishing, 2020.

[23] G.P. Ivantsov. Temperature field around a spherical, cylindrical, and needle-shaped crystal, growing in a pre-cooled melt. *Dokl. Akad. Nauk SSSR*, 58(4):567 – 569, 1947.

[24] Huang W., Geng X., and Zhou . Primary spacing selection of constrained dendritic growth. *Journal of Crystal Growth*, 134(1):105–115, 1993.

[25] S. H. Han and R. Trivedi. Primary spacing selection in directionally solidified alloys. *Acta Metallurgica et Materialia*, 42(1):25–41, 1994.

[26] W. Wang, P. D. Lee, and M. McLean. A model of solidification microstructures in nickel-based superalloys: predicting primary dendrite spacing selection. *Acta materialia*, 51(10):2971–2987, 2003.

[27] P.-A. Geslin, C.-H. Chen, A. M. Tabrizi, and A. Karma. Dendritic needle network modeling of the columnar-to-equiaxed transition. part i: two dimensional formulation and comparison with theory. *Acta Materialia*, 202:42–54, 2021.

[28] J. A. Warren and J. S. Langer. Stability of dendritic arrays. *Physical Review A*, 42(6):3518, 1990.

[29] J. D. Hunt. Solidification and casting of metals. *Metals Society, London*, 3:3–9, 1979.

[30] W. Kurz and D. J. Fisher. Dendrite growth at the limit of stability: tip radius and spacing. *Acta Metallurgica*, 29(1):11–20, 1981.

[31] Ch.-A. Gandin and M. Rappaz. A coupled finite element-cellular automaton model for the prediction of dendritic grain structures in solidification processes. *Acta Metallurgica et Materialia*, 42(7):2233–2246, 1994.

[32] D. Tourret and A. Karma. Growth competition of columnar dendritic grains: A phase-field study. *Acta Materialia*, 82:64–83, 2015.

[33] D. Tourret, Y. Song, A. J. Clarke, and A. Karma. Grain growth competition during thin-sample directional solidification of dendritic microstructures: A phase-field study. *Acta Materialia*, 122:220–235, 2017.

[34] A. Pineau, G. Guillemot, D. Tourret, A. Karma, and Ch.-A. Gandin. Growth competition between columnar dendritic grains–cellular automaton versus phase field modeling. *Acta Materialia*, 155:286–301, 2018.

[35] D. Walton and B. Chalmers. The origin of the preferred orientation in the columnar zone of ingots. *Trans. Metall. Soc. AIME*, 215:3–13, 1959.